AGU ADVANCING EARTH AND SPACE SCIENCES

Geophysical Research Letters

RESEARCH LETTER
10.1029/2023GL106485

Velocity and Temperature Dependence of Steady-State Friction of Natural Gouge Controlled by Competing Healing Mechanisms

Shiying Nie[1] and Sylvain Barbot[1]

[1]University of Southern California, Los Angeles, CA, USA

Key Points:

- The dependence of natural gouge friction on temperature and velocity cannot be captured by empirical laws with constant coefficients
- The competition of healing mechanisms explains a velocity- and temperature-controlled transition between velocity-weakening and hardening
- The constitutive law explains the mechanics of natural gouge from various tectonic settings, allowing scaling up from laboratory to nature

Supporting Information:

Supporting Information may be found in the online version of this article.

Correspondence to:

S. Nie,
shiyingn@usc.edu

Citation:

Nie, S., & Barbot, S. (2024). Velocity and temperature dependence of steady-state friction of natural gouge controlled by competing healing mechanisms. *Geophysical Research Letters*, *51*, e2023GL106485. https://doi.org/10.1029/2023GL106485

Received 20 SEP 2023
Accepted 29 APR 2024

Author Contributions:

Conceptualization: Shiying Nie, Sylvain Barbot
Data curation: Shiying Nie
Formal analysis: Shiying Nie, Sylvain Barbot
Funding acquisition: Sylvain Barbot
Investigation: Shiying Nie, Sylvain Barbot
Methodology: Shiying Nie, Sylvain Barbot
Project administration: Sylvain Barbot
Resources: Shiying Nie, Sylvain Barbot
Software: Shiying Nie
Supervision: Sylvain Barbot

Abstract The empirical rate- and state-dependent friction law is widely used to explain the frictional resistance of rocks. However, the constitutive parameters vary with temperature and sliding velocity, preventing extrapolation of laboratory results to natural conditions. Here, we explain the frictional properties of natural gouge from the San Andreas Fault, Alpine Fault, and the Nankai Trough from room temperature to ∼300°C for a wide range of slip-rates with constant constitutive parameters by invoking the competition between two healing mechanisms with different thermodynamic properties. A transition from velocity-strengthening to velocity-weakening at steady-state can be attained either by decreasing the slip-rate or by increasing temperature. Our study provides a framework to understand the physics underlying the slip-rate and state dependence of friction and the dependence of frictional properties on ambient physical conditions.

Plain Language Summary The physics of friction is crucial to understanding fault mechanics, impacting virtually every aspect of earthquake initiation, propagation, and associated hazards. The mechanics of active fault zones exhibit a complex dependence on temperature and sliding velocity among other factors. The frictional resistance of natural gouge can be explained by empirical rate- and state-dependent friction laws for a limited range of conditions. However, explaining the non-stationary frictional behavior of gouge friction and extrapolation of laboratory constraints to natural conditions remains challenging. In this study, we describe a constitutive law that predicts the velocity of sliding of natural gouge based on applied shear stress, effective confining pressure, and the ambient temperature of the fault. The transition from stable to unstable sliding is controlled by the competition between micro-mechanisms of deformation within the gouge that dominate in distinct ranges of temperature and slip-rate. Once calibrated to mechanical data for a specific lithology and confining pressure, the model explains the temperature and slip-rate control on fault stability, allowing extrapolation of laboratory data to natural conditions.

1. Introduction

The slip-rate and state dependence of friction is a key feature of fault mechanics that enables runaway instabilities and the recurrence of earthquakes (Dieterich, 1972, 1978). The unstable nature of rock friction is widely recognized as the origin of stick-slip instabilities in natural faults (Brace & Byerlee, 1966; Byerlee & Brace, 1968; Ohnaka & Shen, 1999; Scholz, 1998), allowing laboratory analogs, down-scaled versions of earthquakes (Latour et al., 2013; McLaskey, 2019). The frictional behavior of rocks may be described by constitutive laws calibrated with laboratory observations that predict the slip-rate based on shear stress and one or more state variables representing the evolving texture of fault gouge (Dieterich, 1979a, 1979b, 1981; Gu et al., 1984; Ruina, 1983; Rice & Ruina, 1983).

Empirical friction laws capture the direct velocity dependence of friction and the transient phase that follows perturbations of shear stress, normal stress, or temperature (Chester, 1994; Dieterich, 1979a; Linker & Dieterich, 1992), reproducing experimental data for many lithologies in a wide range of hydrothermal settings (e.g., Blanpied et al., 1995; den Hartog et al., 2021; He et al., 2007; Niemeijer et al., 2016; Okuda et al., 2023; Saffer & Marone, 2003; Zhang et al., 2017). Friction laws enable numerical modeling of natural faults (e.g., Barbot, 2020; Barbot et al., 2012; Julve et al., 2023; Liu et al., 2020; Qiu et al., 2016; Sathiakumar & Barbot, 2021; Shi et al., 2022; Tse & Rice, 1986; Veedu & Barbot, 2016), successfully explaining a variety of fault behaviors, encompassing creep, slow-slip events, and crack-like or pulse-like seismic ruptures (e.g., Barbot, 2019b; Cattania & Segall, 2019; Lapusta & Rice, 2003; Nie & Barbot, 2021, 2022; Wang & Barbot, 2023).

10.1029/2023GL106485

Validation: Shiying Nie
Visualization: Shiying Nie, Sylvain Barbot
Writing – original draft: Shiying Nie
Writing – review & editing: Shiying Nie, Sylvain Barbot

The frictional parameters vary widely depending on hydrothermal conditions, slip-rate, pore-fluid and confining pressure, and other factors in laboratory experiments, even for a given lithology. For example, phyllosilicate-rich natural gouge from the Alpine Fault, Nankai Trough, and the Central San Andreas Fault (CSAF) (Boulton et al., 2014, 2018; Carpenter et al., 2015; den Hartog et al., 2012; Moore et al., 2016; Niemeijer et al., 2016; Tesei et al., 2014) consistently show a drastic reduction of the strengthening effect or even a transition from velocity-strengthening to velocity-weakening at steady-state with increasing temperature and/or decreasing slip-rate (Figure 1). The velocity dependence of frictional stability can be captured using a cut-off velocity in the friction law (e.g., Matsuzawa et al., 2010; Okubo, 1989; Shibazaki et al., 2010), but this approach does not incorporate the temperature dependence. Despite the importance of these effects on fault dynamics, the origin of the different regimes of stability is still poorly understood, hindering ongoing efforts to build physical models of the seismic cycle consistent with rock mechanics.

In this study, we use a physics-based constitutive model of rate- and state-dependent friction based on the competition between multiple healing mechanisms (Barbot, 2022) to capture the variations of frictional properties of natural gouge with temperature and slip-rate under constant coefficients. In the next section, we describe the details of the constitutive framework. We then calibrate the model to experimental data from gouge samples cored from the San Andreas Fault Observatory at Depth (SAFOD) that document the frictional behavior from room temperature to 250°C and within three orders of magnitude of slip-rates from a few nanometers to micrometers per second (Moore et al., 2016). Finally, we show that the constitutive model applies to a variety of natural rock samples under varying parametric configurations, including gouge from the South Alpine Fault in New Zealand (Barth et al., 2013), the Alpine Fault Deep Fault Drilling Project (Boulton et al., 2014), the Zuccale Fault in Italy (Collettini et al., 2011), and the Nankai Trough (den Hartog et al., 2012) from room temperature to about 300°C and slip-rate ranging from nanometers to millimeters per second. The model provides comprehensive predictions for different slip-rate and temperature regimes of fault stability simultaneously by incorporating the competition between healing mechanisms, allowing extrapolation of laboratory data to natural fault conditions and more realistic simulations of the seismic cycle.

2. Constitutive Framework

To explain the velocity and temperature control of the steady-state velocity dependence of friction of natural fault gouge, we consider a thermally activated constitutive law based on the real area of contact and the healing of micro-asperities (Barbot, 2019a, 2022, 2023). The constitutive law for cataclastic flow describes the frictional strength in isobaric conditions as

$$\mu = \mu_0 \left(\frac{V}{V_0}\right)^{\frac{1}{n}} \left(\frac{d}{d_0}\right)^{\frac{m}{n}} \exp\left[\frac{Q}{nR}\left(\frac{1}{T} - \frac{1}{T_0}\right)\right], \tag{1}$$

where μ is the frictional resistance controlled by the instantaneous slip-rate V and the temperature T. The representative size of micro-asperities d corresponds to the local radius of curvature at contact junctions and constitutes a state variable for the evolving texture of the gouge layer. The constants $V_0 = 1$ μm/s, $d_0 = 1$ μm, and $T_0 = 25$°C represent reference values of slip-rate, micro-asperity size and ambient temperature, respectively. The reference friction coefficient μ_0 is a material property corresponding to the ratio of plowing to indentation hardness (Bowden & Tabor, 1950, 1964). The coefficients n and m are the stress and microasperity-size power exponents, respectively. The exponential term corresponds to an Arrhenius activation with the energy and temperature of activation Q and T_0, respectively, involving the universal gas constant R. As the laboratory data considered in this study is limited to up to 300°C at constant pore fluid and confining pressure, Equation 1 incorporates only a single mechanism of deformation and, therefore, does not capture the brittle-to-ductile transition observed at higher temperatures and lower slip-rates (Blanpied et al., 1995; den Hartog et al., 2012; Niemeijer et al., 2016; Okuda et al., 2023). Capturing the brittle-to-flow transition requires a constitutive model dependent on multiple deformation mechanisms (Barbot, 2023; Barbot & Zhang, 2023). Given the isobaric experimental conditions considered in this study, we also ignore the nonlinear direct and evolutionary effects of normal stress (Barbot, 2024).

The evolution of the effective asperity size incorporates time-dependent healing by multiple micro-physical mechanisms and slip-dependent comminution by grain fracturing and contact rejuvenation (Barbot, 2022). The corresponding evolution law in isobaric conditions can be cast in additive form, following

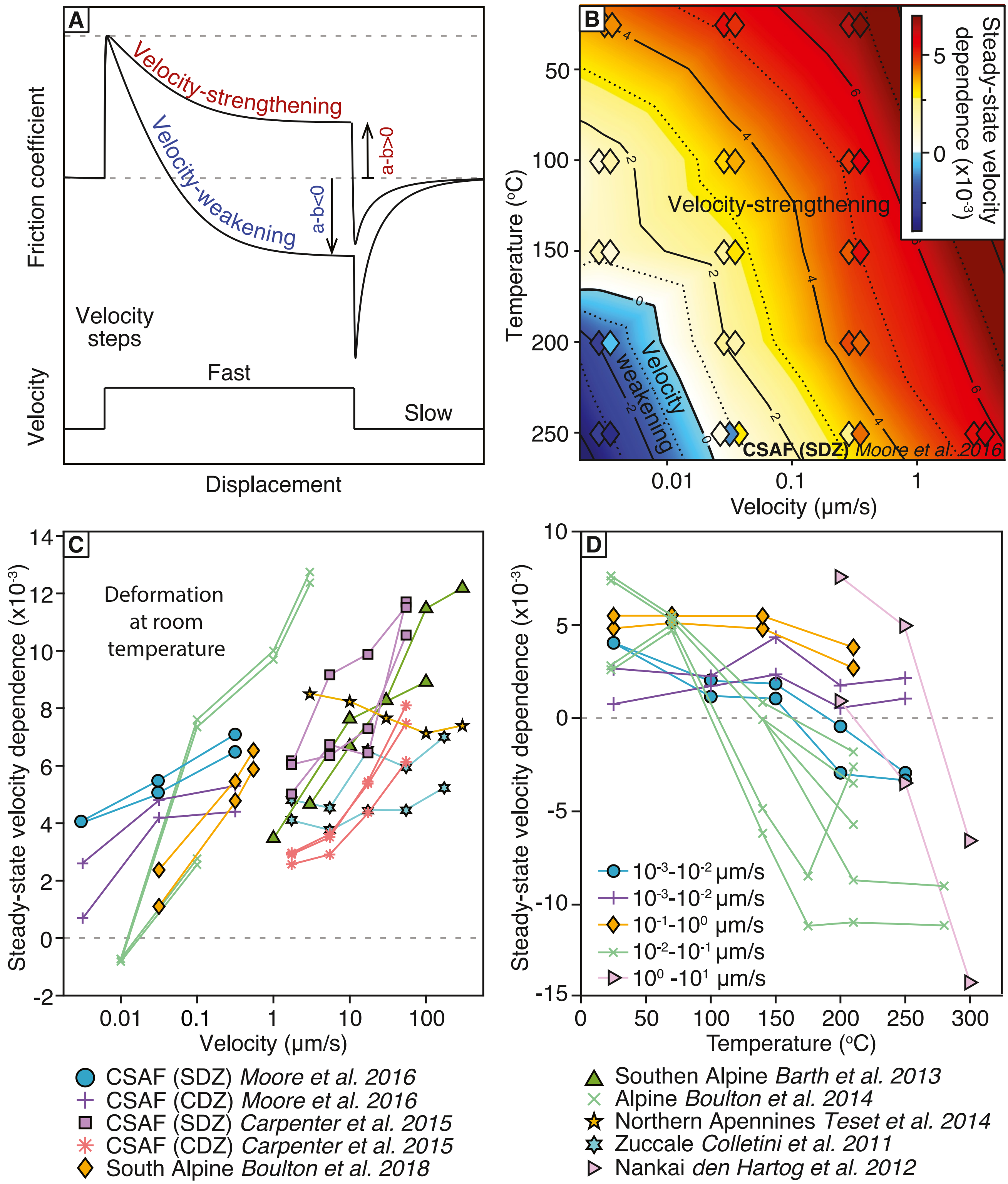
A
Velocity-strengthening
Velocity-weakening
a-b>0
a-b<0
Friction coefficient
Velocity steps
Fast
Slow
Velocity
Displacement
B
Velocity-strengthening
Velocity weakening
Steady-state velocity dependence (x10⁻³)
Temperature (°C)
Velocity (μm/s)
CSAF (SDZ) Moore et al. 2016
C
Deformation at room temperature
Steady-state velocity dependence (x10⁻³)
Velocity (μm/s)
D
10⁻³-10⁻² μm/s
10⁻³-10⁻² μm/s
10⁻¹-10⁰ μm/s
10⁻²-10⁻¹ μm/s
10⁰ -10¹ μm/s
Steady-state velocity dependence (x10⁻³)
Temperature (°C)
CSAF (SDZ) Moore et al. 2016
CSAF (CDZ) Moore et al. 2016
CSAF (SDZ) Carpenter et al. 2015
CSAF (CDZ) Carpenter et al. 2015
South Alpine Boulton et al. 2018
Southen Alpine Barth et al. 2013
Alpine Boulton et al. 2014
Northern Apennines Teset et al. 2014
Zuccale Colletini et al. 2011
Nankai den Hartog et al. 2012

Figure 1.

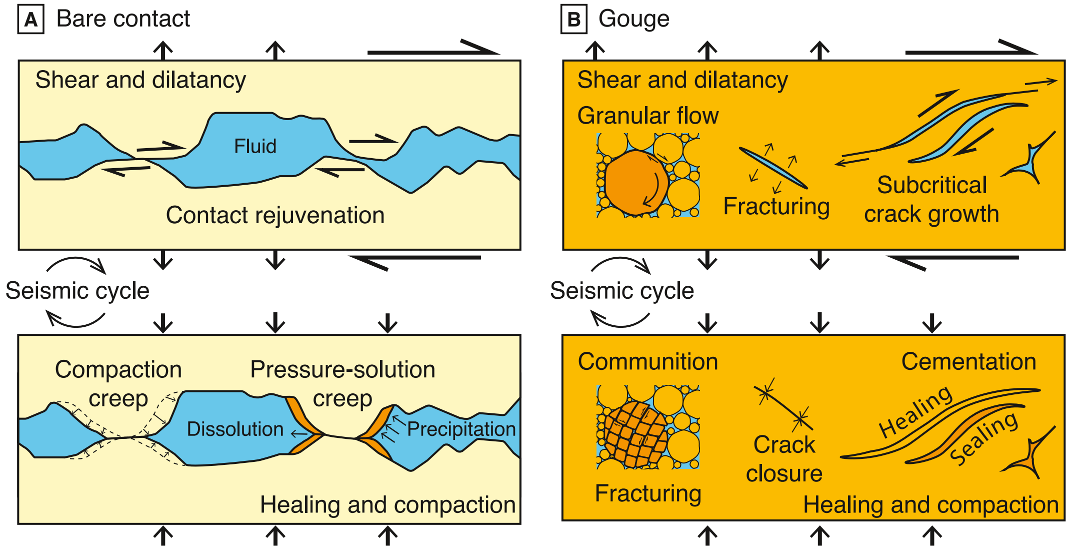

Figure 2. Mechanisms of deformation and healing enabling seismic cycles across a frictional interface. (a) Case of solid-solid or bare contact with contact rejuvenation by dilatant shear during sliding and compaction creep accommodated by viscoelasticity or pressure-solution creep during relocking. (b) Case of solid-gouge-solid contact where granular flow, fracturing, and subcritical crack growth accommodate dilatant shear and comminution. The closure/cementation of cracks enables healing of the interface. Each mechanism acting on different minerals is associated with specific constitutive properties. The deformation associated with healing and contact rejuvenation is anelastic and proceeds as a time-dependent or slip-dependent processes.

$$\frac{\dot{d}}{d} = \sum_{k=1}^{N} \frac{G_k}{p_k d^{p_k}} - \frac{\lambda V}{2h}, \tag{2}$$

where $\dot{d}$ is the rate of change of micro-asperity size. In Equation 2, the first term on the right-hand side corresponds to healing with the micro-asperity size power exponent p_k and the reference growth rate G_k for the healing mechanism $k = 1$ to N. We ignore possible coupling effects between healing mechanisms. The second term on the right-hand side of Equation 2 represents the reduction of asperity size during shear over the gouge thickness h with the characteristic strain $1/\lambda$ due to rejuvenation of the contact population (Figure 2). Alternatively, the evolution law can be expressed in multiplicative form, as

$$\frac{\dot{d}}{d} = \frac{\lambda V}{2h} \ln\left[\sum_{k=1}^{N} \frac{G_k}{p_k d^{p_k}} \Big/ \frac{\lambda V}{2h} \right], \tag{3}$$

involving the difference in the logarithm of the healing and weakening terms. The evolution laws of Equations 2 and 3 may produce different evolutionary effects, for example, varying slip weakening distance (Figure 2 and Figure S1 in Supporting Information S1), but produce the same response at steady-state (Ampuero & Rubin, 2008; Beeler et al., 1994; Bhattacharya et al., 2017, 2022; Nakatani, 2001; Rathbun & Marone, 2013). In both formulations, the healing rate G_k is thermally activated following an Arrhenius formulation, as

$$G_k(T) = G_k^0 \exp\left[-\frac{H_k}{R} \left(\frac{1}{T} - \frac{1}{T_k} \right) \right], \tag{4}$$

Figure 1. Velocity and temperature dependence of friction of natural gouge from laboratory experiments. (a) Schematic of friction evolution during a velocity-jump experiment with possible velocity-strengthening ($a - b > 0$) and velocity-weakening ($a - b < 0$) at steady-state. (b) Measured (diamonds) and interpolated (background color) value of $a - b$ as a function of velocity and temperature for the Southern Deforming Zone sample cored from San Andreas Fault Observatory at Depth in the Central San Andreas Fault. (c) Laboratory measurements of $a - b$ from natural gouge for different loading velocities at room temperature. (d) Variation of $a - b$ under various temperature slip-rate conditions.

where $G_k^0 = (1\,\mu m)^{p_k}/\text{s}$ is the reference growth rate, H_k is the activation enthalpy, and T_k is the activation temperature. The ratio H_k/T_k represents the change of entropy of healing. The evolution of asperity size leads to a change in the real area of contact that modulates the frictional strength. Equivalent evolution laws based on the age of contact that fall in the aging-law and slip-law end-members are discussed in Appendix A.

The healing mechanisms are defined by their distinct thermo-mechanical parameters affected by grain shape, composition, and deformation process (Barbot, 2022; Sleep, 1994, 2006). Healing associated with compaction creep may occur by subcritical crack growth (H. Atkinson, 1988), pressure-solution creep (Gratier et al., 2009), intra-granular deformation (Hirth & Tullis, 1992), and closure of cracks at different rates depending on mineralogy, texture, and temperature (Figure 2). Additional healing may occur without significant fault-perpendicular shortening by crack healing, crack sealing, and cementation of the pore space (Andreani et al., 2004; Gratier et al., 2003; Putnis & Mauthe, 2001).

Considering two healing mechanisms, that is, using $N = 2$ in Equation 2 or Equation 3, we obtain velocity-weakening and velocity-strengthening friction at steady-state in different velocity and temperature regimes controlled by the growth rates and thermodynamic properties of each mechanism. The dominant healing mechanism is associated with the largest grain size at steady-state, which depends on temperature and slip-rate (Figure S2 in Supporting Information S1). When one mechanism dominates, the associated strain-rate can be orders of magnitude higher than the other. However, the transition between healing mechanisms leads to a gradual change of steady-state velocity dependence within specific ranges of temperatures and slip-rates.

3. Constitutive Properties of San Andreas Fault Gouge

We first focus the analysis on laboratory experiments on gouge samples from the San Andreas Fault at SAFOD, which offered direct access to the local creeping segment, allowing the study of the mechanical, compositional, and frictional properties of fault gouge (Carpenter et al., 2015; Lockner et al., 2011; Thurber et al., 2004). The borehole crossed two creeping strands of the CSAF at about 3 km depth (Zoback et al., 2010, 2011). Samples from the Southern Deforming Zone (SDZ) and Central Deforming Zone are rich in phyllosilicates, including saponite, corrensite, and serpentinite, and exhibit steady-state velocity-strengthening at room temperature. The slightly stronger SDZ strand, with a lower phyllosilicate and higher quartz and feldspar content, becomes velocity-weakening under elevated temperature or sufficiently low velocity (Moore et al., 2016).

We utilize the mechanical data from velocity-step experiments on the SDZ samples for three orders of magnitude of slip-rates, from nanometers to micrometers per second, from room temperature at 25 to 250°C in isobaric conditions, with a constant effective normal stress of $\bar{\sigma} = 100\,\text{MPa}$ (Moore et al., 2016). The loading rate of the slowest experiments is close to the long-term slip-rate of the San Andreas Fault (Barbot et al., 2009, 2013), approaching the conditions of rupture nucleation. We first use the RSFit3000 methodology (Skarbek & Savage, 2019) to derive the empirical rate- and state-dependent parameters (Ruina, 1983), including the reference friction coefficient μ_0, a, b, the characteristic weakening distance L, and the system stiffness k (Figure S3 in Supporting Information S1). A key aspect of rate- and state-dependent friction laws is the steady-state velocity dependence parameter, characterized by

$$a - b = \frac{\partial \mu_{ss}}{\partial \ln V}, \tag{5}$$

where μ_{ss} is the steady-state friction coefficient, defined as the ratio of the shear and effective normal stresses, and V is the slip-rate across the fault. The sign of $a - b$ controls frictional stability, that is, the potential of a fault to generate dynamic ruptures (Figure 1a). Steady-state velocity-weakening friction, which occurs for $a - b < 0$, allows the nucleation and propagation of earthquakes and slow-slip events. In contrast, velocity-strengthening condition, with $a - b > 0$, promotes stable sliding, manifested as fault creep (Harris, 2017) or afterslip following mainshock ruptures (Marone et al., 1991). The constitutive parameters are scattered with a small dynamic range, consistent with a single deformation mechanism. However, there is a clear dependence of the state-dependence parameter b on temperature and velocity, indicating changes in the underpinning evolutionary process (Figure S3 in Supporting Information S1). The corresponding trend of $a - b$ shows a clear sensitivity to slip-rate and temperature, delineating two distinct stability regimes (Figure 3). The velocity-weakening regime operates at high temperatures and low slip rates.

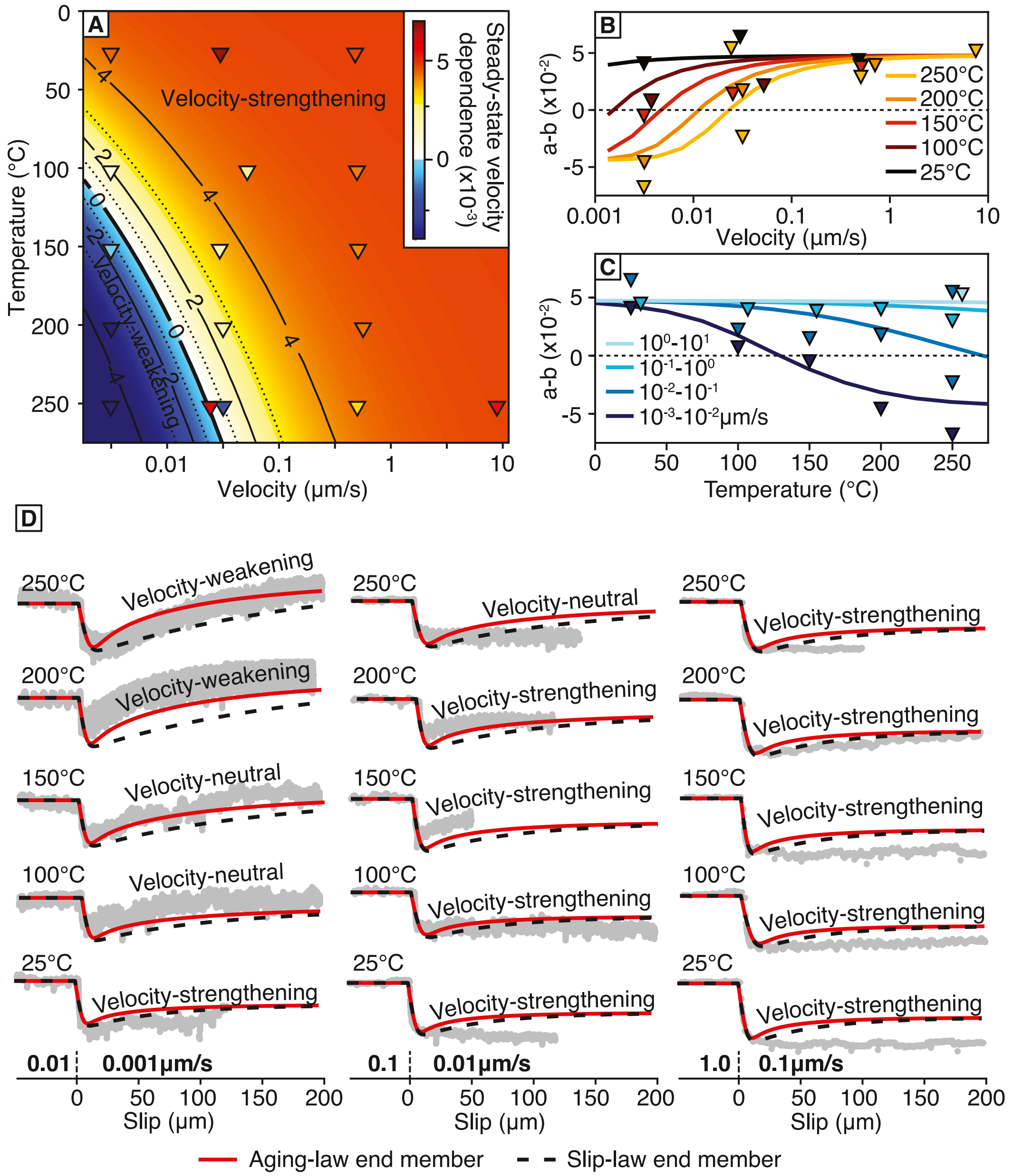

Figure 3. Comparison between simulated and measured frictional data for samples from the Southern Deforming Zone of the San Andreas Fault Observatory at Depth. (a) Comparison between simulated (background color) and measured (colored triangles) steady-state velocity-dependence parameter $a - b$. (b) Simulated (lines) and regressed (triangles) $a - b$ parameters as a function of velocity colored by temperature. (c) Simulated (lines) and regressed (triangles) $a - b$ parameters as a function of temperature colored by velocity. (d) Comparison of the synthetic (lines) and raw friction coefficient measurements (gray dots). The red solid lines and black dashed lines denote simulations conducted using Equations 2 and 3, respectively.

To explain the experimental data, recognizing the various merits and shortcomings of the slip law and aging law end-members (Beeler et al., 1994; Bhattacharya et al., 2022, and references therein), we conduct numerical simulations of the velocity jump experiments with a spring-slider assembly with the constitutive laws of Equations 1 and 2 and separately with Equations 1 and 3. The conservation of linear momentum in isobaric condition implies

$$\dot{\mu}\bar{\sigma} = -k(V - V_L) \tag{6}$$

Table 1
Constitutive and Physical Parameters of the Simulated Velocity-Step Experiments on the San Andreas Fault Observatory at Depth SDZ Sample Shown in Figure 3

Parameter	Symbol	Value
Direct effect		
Reference friction coefficient	μ_0	0.21
Reference asperity size	d_0	1 μm
Reference velocity	V_0	1 μm/s
Effective normal stress	$\bar{\sigma}$	100 MPa
Stress power exponent	n	24 ± 5
Asperity-size power exponent	m	1.64 ± 0.2
Activation energy	Q	85 ± 15 kJ/mol
Reference temperature	T_0	25°C
Evolutionary effects		
Size-sensitivity exponent	p_1	1.1
	p_2	3.6
Activation enthalpy	H_1	80 ± 15 kJ/mol
	H_2	195 ± 45 kJ/mol
Activation temperature	T_1	286°C
	T_2	106°C
Reference strain	$1/\lambda$	0.1
Gouge thickness	h	1 mm

Note. The uncertainties correspond to plus or minus a standard deviation. The parameters $d_0 = 1$ μm, $V_0 = 1$ μm/s, and $T_0 = 25$°C represent scaling factors, not constitutive parameters per se. The reference friction coefficient μ_0 is a material property corresponding to the ratio of plowing to indentation hardness. The gouge thickness $h = 1$ mm is a laboratory setting.

where k is the stiffness of the system and V_L represents the imposed loading rate, which varies from V_1 to V_2 across a velocity step (Figure S4 in Supporting Information S1). As the loading rate barely exceeds micrometers per second and the gouge is conditionally stable at the experimental conditions, we ignore the radiation of seismic waves. We estimate the empirical parameter $a - b$ using a numerical approximation of Equation 5. Conducting such experiments for various temperatures and slip rates allows us to calculate the residuals with the laboratory observations. We optimize 10 constitutive parameters (μ_0, n, m, and Q for the direct effect and p_1, p_2, H_1, H_2, T_1, and T_2 for the evolutionary effects) by grid search to minimize the root mean square of the residuals with about 56 measurements of frictional resistance at steady-state and 33 measurements of $a - b$ (Figures S5 and S6 in Supporting Information S1).

The frictional parameters for the SDZ gouge are best explained by the power exponents $n = 24 \pm 5$, $m = 1.64 \pm 0.2$ in the flow law of Equation 1. The reference friction coefficient $\mu_0 = 0.21$ and the activation energy $Q = 85 \pm 15$ kJ/mol are constrained by the average frictional resistance at steady-state (Figure S5 in Supporting Information S1). The distinct regimes of stability are controlled by the competition of healing mechanisms with activation enthalpies $H_1 = 80 \pm 15$ kJ/mol and $H_2 = 195 \pm 45$ kJ/mol. The absolute value of the activation temperatures cannot be determined with the data available, but the ratio $T_1/T_2 = 1.51$ is well constrained. The size power exponents for healing $p_1 = 1.1$ and $p_2 = 3.6$ trade off with each other, but fall within the expectation of $p_1 < m$ for steady-state velocity-weakening and $p_2 > m$ for velocity strengthening. The best-fitting parameters are summarized in Table 1.

The constitutive framework explains the transition between velocity-weakening and velocity-strengthening at steady-state controlled by slip-rate and temperature (Figure 3). The model does not resolve a few velocity-step experiments well because a single set of constitutive parameters is used for all experimental data. In the higher velocity and/or lower temperature range, the velocity-strengthening healing mechanism with $p_1 > m$ controls the frictional behavior. In the complementary range with a velocity-weakening behavior, the second healing mechanism with $p_2 < m$ dominates (Figure 3a). These results are corroborated by the evolution of the friction coefficient, whereby only the velocity step from 10^{-2} to 10^{-3} μm/s at 200 and 250°C exhibits velocity-weakening (Figure 3d).

The thermodynamic properties of the SDZ samples provide new insights into the dominant healing mechanisms. The activation energy $H_1 = 80$ kJ/mol is compatible with a variety of healing mechanisms operating in wet conditions, including subcritical crack growth, pressure solution, and crack healing or crack sealing (B. K. Atkinson, 1984; Barbot, 2022; Brantley et al., 2008; Marty et al., 2015; Niemeijer et al., 2002; Rimstidt & Barnes, 1980). With the activation energy $H_2 = 195$ kJ/mol, the second healing mechanism may involve the viscoelastic collapse of a weak mineral phase within the gouge (Barbot, 2022; Hirth et al., 2001; Kronenberg et al., 1990; Rybacki & Dresen, 2000).

4. Application to Other Fault Gouges

We now consider the velocity-step experiments conducted on natural samples from the South Alpine Fault (Barth et al., 2013; Boulton et al., 2014, 2018), CSAF (Carpenter et al., 2015), Zuccale Fault (Collettini et al., 2011; Kaproth & Marone, 2013), and Nankai Trough (den Hartog et al., 2012) at varying slip rates, temperatures, or both. Most samples exhibit a predominantly velocity-strengthening behavior in the experimental conditions, consistent with the presence of hydrous minerals and clays in all samples (e.g., smectite, chlorite, illite, saponite). However, a few cases exhibit velocity-weakening at steady-state for sufficiently low velocity (e.g., Figures 4e, 4h, and 4i). Regardless, all samples exhibit increasing stability with increasing slip-rate or decreasing temperature.

10.1029/2023GL106485

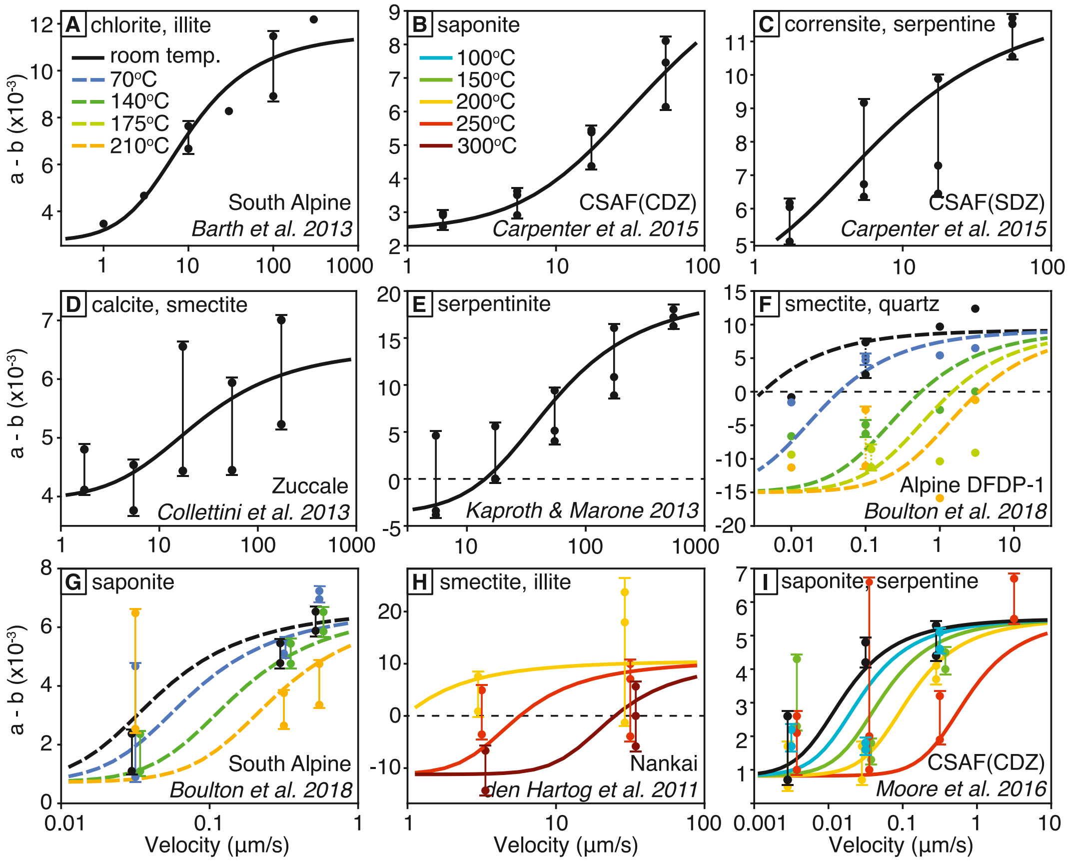

Figure 4. Comparison between simulated (lines) and laboratory-derived (dots) velocity dependence parameter ($a - \mathrm{b}$) of natural samples from (a) South Alpine fault (Barth et al., 2013), (b) and (c) Central Deforming Zone (CDZ) and Southern Deforming Zone of Central San Andreas Fault (CSAF), respectively (Carpenter et al., 2015), (d) Zuccale Fault (Collettini et al., 2011), (e) lizardite-rich serpentinite sample (Kaproth & Marone, 2013), (f) Alpine DFDP-1 sample (Boulton et al., 2014), (g) South Alpine outcrop (Boulton et al., 2018), (h) Nankai (simulated) (den Hartog et al., 2012), and (i) CSAF CDZ (Moore et al., 2016). Colors represent experiments under different temperatures. The dashed line is for $a - b = 0$. Additional results for serpentinite gouge Pozzi et al. (2023) are included in Figure S7 of Supporting Information S1.

Using the procedure described in the previous section, we obtain constitutive parameters that explain the evolution of the steady-state velocity dependence parameters $a - b$ with temperature and slip-rate (Figure 4), as summarized in Table 2. As these experiments document a limited range of slip rates and temperatures, a wide range of thermodynamic properties can explain the mechanical data equally well. The activation enthalpy varies in the range 50–80 kJ/mol and 80–150 kJ/mol for the low- and high-temperature healing mechanisms, respectively, which is typical in the brittle regime. For example, hornblende (Liu & He, 2020), pyroxene (Tian & He, 2019), and natural gouges (An et al., 2020; Valdez et al., 2019; den Hartog et al., 2021) in wet conditions feature an activation enthalpy within 20–65 kJ/mol (Barbot, 2022). Similarly, wet Westerly granite (Blanpied et al., 1995), basalt (Okuda et al., 2023), and cataclasite gouge from the Alpine Fault (Niemeijer et al., 2016) exhibit an activation enthalpy for healing in the range 30–55 kJ/mol (Barbot, 2023). The presence of mechanisms characterized by activation energy greater than 100 kJ/mol suggests the activation of compaction creep of anhydrous minerals. For instance, the sample from the Zuccale Fault contains calcite (Collettini et al., 2011), which shows activation energies of 145–250 kJ/mol for viscoelastic flow (Holyoke et al., 2013). Samples from SAFOD include quartz and feldspar (Carpenter et al., 2015; Moore et al., 2016) that showcase activation energies for viscoelastic flow of 150–600 kJ/mol (Rybacki & Dresen, 2000) and 135–240 kJ/mol (Rutter & Brodie, 2004a, 2004b), respectively. Conversely, the low activation energy of healing under specific conditions suggests the deformation of phyllosilicates or other weak minerals (Barbot, 2022; Mares & Kronenberg, 1993; Mariani et al., 2006; Shea & Kronenberg, 1992).

Table 2
Constitutive Parameters of Natural Gouge Constrained by Velocity-Step Experiments (Figures 3 and 4)

Fault gouge	Mineral assembly	n	m	p_1	p_2	H_1	H_2	T_1	T_2	Reference
Alpine Fault	Chlorite, illite	29	0.8	1.0	2.5	80	150	217	338	Barth et al. (2013)
	Smectite, quartz, K-feldspar	17	1.9	1.3	2.7	60	80	200	150	Boulton et al. (2014)
	Saponite, serpentine	53	0.9	1.0	3.1	50	180	206	106	Boulton et al. (2018)
San Andreas (CDZ)	Saponite	28	1.0	1.2	2.7	80	150	217	325	Carpenter et al. (2015)
	Saponite, serpentine	62	0.9	1.0	2.8	50	180	206	110	Moore et al. (2016)
San Andreas (SDZ)	Corrensite, serpentine	26	1.0	1.2	2.7	80	150	217	275	Carpenter et al. (2015)
Zuccale Fault	Calcite, smectite	59	0.6	1.1	2.5	80	150	217	308	Collettini et al. (2011)
	Lizardite-rich serpentinite	15	1.1	1.0	2.7	80	150	165	308	Kaproth and Marone (2013)
Nankai Trough	Smectite, illite, chlorite	29	1.6	1.0	4.1	80	100	277	278	den Hartog et al. (2012)

Note. The activation energies H_1 and H_2 are in kJ/mol. The activation temperatures T_1 and T_2 are in degrees Celsius.

5. Discussion

As evidenced by an abundance of laboratory experiments, the frictional behavior of natural gouge is complex, involving different stability regimes based on ambient temperature and instantaneous slip rate. The mechanics of gouge friction cannot be explained using empirical friction laws at constant parameters, at least not as previously defined (see Appendix A). In contrast, the constitutive framework described in Section 2 captures the frictional behavior of natural gouge for a wide range of rocks upon parametric adjustments based on lithology and confining or pore-fluid pressures. The constitutive model employed here applies within a nominal range of temperatures and slip rates that exclude the brittle-ductile transition. These results facilitate the scaling of laboratory observations up to natural fault conditions within the relatively low temperatures of the middle and upper crust or the thick sedimentary layers of accretionary prisms at subduction zones.

The non-stationary properties of gouge friction documented in the laboratory and captured in the constitutive model imply complex dynamics of natural faults. The unstable friction of phyllosilicate-rich gouge at a sufficiently low slip rate and increased stability at intermediate velocity is particularly relevant to creeping faults. Although the CSAF exhibits primarily aseismic slip (Barbot et al., 2013; Scott et al., 2020), creep is spatio-temporally variable and episodic (Khoshmanesh & Shirzaei, 2018; Khoshmanesh et al., 2015; Titus et al., 2006). This phenomenon is compatible with phyllosilicate gouge friction, which is often found to be velocity-weakening at low slip speed (e.g., Pozzi et al., 2023), allowing nucleation of instabilities, but velocity-strengthening at higher velocity, inhibiting the transition to seismic rupture propagation. The slip-rate dependence of gouge stability may also explain shallow slow-slip events above the seismogenic zone of the San Andreas Fault (Wei et al., 2013) and the North Anatolian Fault (Kaneko et al., 2013). Furthermore, phyllosilicates typically exhibit a strong increase of the effective friction coefficient with normal stress (Moore & Lockner, 2008). Generalizing the constitutive equations to incorporate the effect of normal stress (Barbot, 2024) explains this behavior (Figure S8 in Supporting Information S1).

The complex frictional behavior of natural gouge may explain the non-stationary creeping behavior observed in other faults, such as the Laohushan segment of the Haiyuan fault (Jolivet et al., 2012, 2013; Li et al., 2021), and the Pütürge and Palu segments of the East Anatolian Fault (Bletery et al., 2020; Cakir et al., 2023; Ragon et al., 2021). The temperature dependence of gouge friction also implies variations in fault behavior with depth, including the prevalence of a shallow slip deficit during large earthquakes (Barbot et al., 2023; Fialko et al., 2005; Qiu et al., 2020) and variations of interseismic coupling as a function of depth (e.g., Jolivet et al., 2015).

6. Conclusion

We describe a constitutive framework for gouge friction that explains the widely observed velocity and temperature dependence of effective mechanical properties. The competition between thermally activated healing mechanisms and weakening by contact rejuvenation leads to distinct stability regimes with a tendency for increased stability with increasing slip rate or decreasing temperature. The model applies to a range of temperatures and slip-rates within the brittle field for phyllosilicate-rich gouge. Considering additional deformation mechanisms is required to capture the brittle-ductile transition (Barbot, 2023; Barbot & Zhang, 2023). The constitutive model explains the frictional behavior of natural gouge from the San Andreas Fault, Zuccale Fault, Alpine Fault, and the Nankai Trough under varying parametric configurations, allowing the extrapolation of laboratory data to natural fault conditions within the middle and top crust. If the effects of temperature and slip rate on the frictional resistance are now better understood, the remaining controls of varying pore-fluid pressure remain elusive. Further experimental work is needed to describe the properties of a wide range of rocks and calibrate the model for different tectonic contexts and hydrothermal conditions.

Appendix A: Formulations Based on the Age of Contact

In this Appendix, we describe how the empirical evolution laws based on the age of contact can be modified to enable a stability transition with increasing slip-rate. For simplicity, we discuss the constitutive behavior at isobaric condition. The temperature effects are captured in the temperature dependence of G_i. The evolutionary effects of rate- and state-dependent friction can be described using the age of contact (Dieterich, 1979a, 1979b; Ruina, 1983). The relationship between size and age of contact is well-defined when a single healing mechanism operates (Barbot, 2019a). However, with the competition of multiple healing mechanisms, the apparent age depends on the healing rate of reference (Barbot, 2022).

Taking arbitrarily the first healing mechanism as a reference and assuming two distinct healing mechanisms, we define the apparent age of contact as (Barbot, 2019a)

$$\theta = \frac{d^{p_1}}{G_1}. \tag{A1}$$

Defining the characteristic weakening distance as a fraction of the gouge thickness (Barbot, 2019a)

$$L = \frac{2h}{\lambda p_1}, \tag{A2}$$

the evolution law of Equations 2 and 3 can be written as a function of the age of contact. Specifically, Equation 2 becomes

$$\dot{\theta} = 1 + \alpha\theta^{\beta} - \frac{V\theta}{L}, \tag{A3}$$

and Equation 3 becomes

$$\dot{\theta} = -\frac{V\theta}{L}\ln\left[\frac{V\theta}{L}\Big/\left(1 + \alpha\theta^{\beta}\right)\right]. \tag{A4}$$

The competition of two healing mechanisms introduces a new term associated with the parameters

$$\alpha = \frac{G_2}{rG_1^r} \tag{A5}$$

and

$$\beta = 1 - r \tag{A6}$$

that depend on the ratio of the micro-asperity size power exponents $r = p_2/p_1$. If the second healing mechanism can be neglected, with $G_2 = 0$, then $\alpha = 0$ and Equations A3 and A4 reduce to the aging law and the slip law defined by Ruina (1983), respectively. The correspondence between the apparent age and size of contact indicates how the empirical evolution laws can be modified to capture the temperature and velocity dependence of the stability regime of gouge friction. Although the formulations based on the age of contact are mathematically adequate, they are physically inconsistent due to the ambiguity of the reference healing rate. When multiple healing mechanisms operate, using the size of contact is more appropriate.

Data Availability Statement

The data and computer programs used to create Figures 3 and 4 are available at Nie and Barbot (2024).

Acknowledgments
We thank Virginia Toy and two anonymous reviewers for their helpful comments and suggestions, which have improved the manuscript. This study is supported in part by the National Science Foundation under award number EAR-1848192.

References

Ampuero, J.-P., & Rubin, A. M. (2008). Earthquake nucleation on rate and state faults—Aging and slip laws. *Journal of Geophysical Research*, *113*(B1), B01302. https://doi.org/10.1029/2007JB005082

An, M., Zhang, F., Elsworth, D., Xu, Z., Chen, Z., & Zhang, L. (2020). Friction of Longmaxi shale gouges and implications for seismicity during hydraulic fracturing. *Journal of Geophysical Research*, *125*(8), e2020JB019885. https://doi.org/10.1029/2020JB019885

Andreani, M., Baronnet, A., Boullier, A.-M., & Gratier, J.-P. (2004). A microstructural study of a "crack-seal" type serpentine vein using SEM and TEM techniques. *European Journal of Mineralogy*, *16*(4), 585–595. https://doi.org/10.1127/0935-1221/2004/0016-0585

Atkinson, B. K. (1984). Subcritical crack growth in geological materials. *Journal of Geophysical Research*, *89*(B6), 4077–4114. https://doi.org/10.1029/jb089ib06p04077

Atkinson, H. (1988). Overview no. 65: Theories of normal grain growth in pure single phase systems. *Acta Metallurgica*, *36*(3), 469–491. https://doi.org/10.1016/0001-6160(88)90079-X

Barbot, S. (2019a). Modulation of fault strength during the seismic cycle by grain-size evolution around contact junctions. *Tectonophysics*, *765*, 129–145. https://doi.org/10.1016/j.tecto.2019.05.004

Barbot, S. (2019b). Slow-slip, slow earthquakes, period-two cycles, full and partial ruptures, and deterministic chaos in a single asperity fault. *Tectonophysics*, *768*, 228171. https://doi.org/10.1016/j.tecto.2019.228171

Barbot, S. (2020). Frictional and structural controls of seismic super-cycles at the Japan trench. *Earth Planets and Space*, *72*(1), 63. https://doi.org/10.1186/s40623-020-01185-3

Barbot, S. (2022). A rate-state-and temperature-dependent friction law with competing healing mechanisms. *Journal of Geophysical Research*, *127*(11), e2022JB025106. https://doi.org/10.1029/2022JB025106

Barbot, S. (2023). Constitutive behavior of rocks during the seismic cycle. *AGU Advances*, *4*(5), e2023AV000972. https://doi.org/10.1029/2023AV000972

Barbot, S. (2024). Transient and steady-state friction in non-isobaric conditions. *Geochemistry, Geophysics, Geosystems*, *25*(2), e2023GC011279. https://doi.org/10.1029/2023GC011279

Barbot, S., Agram, P., & De Michele, M. (2013). Change of apparent segmentation of the San Andreas Fault around Parkfield from space geodetic observations across multiple periods. *Journal of Geophysical Research*, *118*(12), 6311–6327. https://doi.org/10.1002/2013JB010442

Barbot, S., Fialko, Y., & Bock, Y. (2009). Postseismic deformation due to the Mw 6.0 2004 Parkfield earthquake: Stress-driven creep on a fault with spatially variable rate-and-state friction parameters. *Journal of Geophysical Research*, *114*(B7), B07405. https://doi.org/10.1029/2008JB005748

Barbot, S., Lapusta, N., & Avouac, J. P. (2012). Under the hood of the earthquake machine: Towards predictive modeling of the seismic cycle. *Science*, *336*(6082), 707–710. https://doi.org/10.1126/science.1218796

Barbot, S., Luo, H., Wang, T., Hamiel, Y., Piatibratova, O., Javed, M. T., et al. (2023). Slip distribution of the February 6, 2023 Mw 7.8 and Mw 7.6, Kahramanmaraş, Turkey earthquake sequence in the East Anatolian fault zone. *Seismica*, *2*(3). https://doi.org/10.26443/seismica.v2i3.502

Barbot, S., & Zhang, L. (2023). Constitutive behavior of olivine gouge across the brittle-ductile transition. *Geophysical Research Letters*, *50*(24), e2023GL105916. https://doi.org/10.1029/2023GL105916

Barth, N., Boulton, C., Carpenter, B., Batt, G., & Toy, V. (2013). Slip localization on the southern alpine fault, New Zealand. *Tectonics*, *32*(3), 620–640. https://doi.org/10.1002/tect.20041

Beeler, N. M., Tullis, T. E., & Weeks, J. D. (1994). The roles of time and displacement in the evolution effect in rock friction. *Geophysical Research Letters*, *21*(18), 1987–1990. https://doi.org/10.1029/94GL01599

Bhattacharya, P., Rubin, A. M., & Beeler, N. M. (2017). Does fault strengthening in laboratory rock friction experiments really depend primarily upon time and not slip? *Journal of Geophysical Research*, *122*(8), 6389–6430. https://doi.org/10.1002/2017JB013936

Bhattacharya, P., Rubin, A. M., Tullis, T. E., Beeler, N. M., & Okazaki, K. (2022). The evolution of rock friction is more sensitive to slip than elapsed time, even at near-zero slip rates. *Proceedings of the National Academy of Sciences*, *119*(30), e2119462119. https://doi.org/10.1073/pnas.2119462119

Blanpied, M. L., Lockner, D. A., & Byerlee, J. D. (1995). Frictional slip of granite at hydrothermal conditions. *Journal of Geophysical Research*, *100*(B7), 13045–13064. https://doi.org/10.1029/95JB00862

Bletery, Q., Cavalié, O., Nocquet, J.-M., & Ragon, T. (2020). Distribution of interseismic coupling along the North and East Anatolian faults inferred from InSAR and GPS data. *Geophysical Research Letters*, *47*(16), e2020GL087775. https://doi.org/10.1029/2020GL087775

Boulton, C., Barth, N. C., Moore, D. E., Lockner, D. A., Townend, J., & Faulkner, D. R. (2018). Frictional properties and 3-D stress analysis of the southern Alpine Fault, New Zealand. *Journal of Structural Geology*, *114*, 43–54. https://doi.org/10.1016/j.jsg.2018.06.003

Boulton, C., Moore, D. E., Lockner, D. A., Toy, V. G., Townend, J., & Sutherland, R. (2014). Frictional properties of exhumed fault gouges in DFDP-1 cores, Alpine Fault, New Zealand. *Geophysical Research Letters*, *41*(2), 356–362. https://doi.org/10.1002/2013GL058236

Bowden, F. P., & Tabor, D. (1950). *The friction and lubrication of Solids, Part I*. Clarendon Press.

Bowden, F. P., & Tabor, D. (1964). *The friction and lubrication of Solids, Part II*. Clarendon Press.

Brace, W., & Byerlee, J. (1966). Stick-slip as a mechanism for earthquakes. *Science*, *153*(3739), 990–992. https://doi.org/10.1126/science.153.3739.990

Brantley, S. L., Kubicki, J. D., & White, A. F. (Eds.). (2008). *Kinetics of water-rock interaction*. Springer. https://doi.org/10.1007/978-0-387-73563-4

Byerlee, J. D., & Brace, W. (1968). Stick slip, stable sliding, and earthquakes—Effect of rock type, pressure, strain rate, and stiffness. *Journal of Geophysical Research*, *73*(18), 6031–6037. https://doi.org/10.1029/JB073i018p06031

Cakir, Z., Doğan, U., Akoğlu, A. M., Ergintav, S., Özarpacı, S., Özdemir, A., et al. (2023). Arrest of the mw 6.8 January 24, 2020 Elaziğ (Turkey) earthquake by shallow fault creep. *Earth and Planetary Science Letters*, *608*, 118085. https://doi.org/10.1016/j.epsl.2023.118085

Carpenter, B., Saffer, D., & Marone, C. (2015). Frictional properties of the active San Andreas Fault at SAFOD: Implications for fault strength and slip behavior. *Journal of Geophysical Research*, *120*(7), 5273–5289. https://doi.org/10.1002/2015JB011963

Cattania, C., & Segall, P. (2019). Crack models of repeating earthquakes predict observed moment-recurrence scaling. *Journal of Geophysical Research*, *124*(1), 476–503. https://doi.org/10.1029/2018JB016056

Chester, F. (1994). Effects of temperature on friction: Constitutive equations and experiments with fault gouge. *Journal of Geophysical Research*, *99*(B4), 7247–7261. https://doi.org/10.1029/93JB03110

Collettini, C., Niemeijer, A., Viti, C., Smith, S. A., & Marone, C. (2011). Fault structure, frictional properties and mixed-mode fault slip behavior. *Earth and Planetary Science Letters*, *311*(3), 316–327. https://doi.org/10.1016/j.epsl.2011.09.020

den Hartog, S., Peach, C. J., de Winter, D. M., Spiers, C. J., & Shimamoto, T. (2012). Frictional properties of megathrust fault gouges at low sliding velocities: New data on effects of normal stress and temperature. *Journal of Structural Geology*, *38*, 156–171. https://doi.org/10.1016/j.jsg.2011.12.001

den Hartog, S., Thomas, M. Y., & Faulkner, D. (2021). How do laboratory friction parameters compare with observed fault slip and geodetically derived friction parameters? Insights from the Longitudinal Valley Fault, Taiwan. *Journal of Geophysical Research*, *126*(10), e2021JB022390. https://doi.org/10.1029/2021JB022390

Dieterich, J. H. (1972). Time-dependent friction in rocks. *Journal of Geophysical Research*, *77*(20), 3690–3697. https://doi.org/10.1029/JB077i020p03690

Dieterich, J. H. (1978). Time-dependent friction and the mechanics of stick-slip. *Pure and Applied Geophysics*, *116*(4–5), 790–806. https://doi.org/10.1007/978-3-0348-7182-2_15

Dieterich, J. H. (1979a). Modeling of rock friction 1. Experimental results and constitutive equations. *Journal of Geophysical Research*, *84*(B5), 2161–2168. https://doi.org/10.1029/JB084iB05p02161

Dieterich, J. H. (1979b). Modeling of rock friction 2. Simulation of preseismic slip. *Journal of Geophysical Research*, *84*(B5), 2169–2175. https://doi.org/10.1029/JB084iB05p02169

Dieterich, J. H. (1981). Constitutive properties of faults with simulated gouge. In J. M. L. N. L. Carter, M. Friedman, & D. W. Stearns (Eds.), *Monograph 24: Mechanical behavior of crustal rocks* (pp. 103–120). AGU. https://doi.org/10.1029/GM024p0103

Fialko, Y., Sandwell, D., Simons, M., & Rosen, P. (2005). Three-dimensional deformation caused by the Bam, Iran, earthquake and the origin of shallow slip deficit. *Nature*, *435*(7040), 295–299. https://doi.org/10.1038/nature03425

Gratier, J.-P., Favreau, P., & Renard, F. (2003). Modeling fluid transfer along California faults when integrating pressure solution crack sealing and compaction processes. *Journal of Geophysical Research*, *108*(B2), 2104. https://doi.org/10.1029/2001jb000380

Gratier, J.-P., Guiguet, R., Renard, F., Jenatton, L., & Bernard, D. (2009). A pressure solution creep law for quartz from indentation experiments. *Journal of Geophysical Research*, *114*(B3), B03403. https://doi.org/10.1029/2008JB005652

Gu, J., Rice, J. R., Ruina, A. L., & Tse, S. T. (1984). Slip motion and stability of a single degree of freedom elastic system rate and state dependent friction. *Journal of the Mechanics and Physics of Solids*, *32*(3), 167–196. https://doi.org/10.1016/0022-5096(84)90007-3

Harris, R. A. (2017). Large earthquakes and creeping faults. *Reviews of Geophysics*, *55*(1), 169–198. https://doi.org/10.1002/2016rg000539

He, C., Wang, Z., & Yao, W. (2007). Frictional sliding of gabbro gouge under hydrothermal conditions. *Tectonophysics*, *445*(3–4), 353–362. https://doi.org/10.1016/j.tecto.2007.09.008

Hirth, G., Tessier, C., & Dunlap, W. J. (2001). An evaluation of quartzite flow laws based on comparisons between experimentally and naturally deformed rocks. *International Journal of Earth Sciences*, *90*(1), 77–87. https://doi.org/10.1007/s005310000152

Hirth, G., & Tullis, J. (1992). Dislocation creep regimes in quartz aggregates. *Journal of Structural Geology*, *14*(2), 145–159. https://doi.org/10.1016/0191-8141(92)90053-y

Holyoke, III, C. W., Kronenberg, A. K., & Newman, J. (2013). Dislocation creep of polycrystalline dolomite. *Tectonophysics*, *590*, 72–82. https://doi.org/10.1016/j.tecto.2013.01.011

Jolivet, R., Lasserre, C., Doin, M.-P., Guillaso, S., Peltzer, G., Dailu, R., et al. (2012). Shallow creep on the Haiyuan fault (Gansu, China) revealed by SAR interferometry. *Journal of Geophysical Research*, *117*(B6), B06401. https://doi.org/10.1029/2011JB008732

Jolivet, R., Lasserre, C., Doin, M.-P., Peltzer, G., Avouac, J.-P., Sun, J., & Dailu, R. (2013). Spatio-temporal evolution of aseismic slip along the Haiyuan fault, China: Implications for fault frictional properties. *Earth and Planetary Science Letters*, *377*, 23–33. https://doi.org/10.1016/j.epsl.2013.07.020

Jolivet, R., Simons, M., Agram, P., Duputel, Z., & Shen, Z.-K. (2015). Aseismic slip and seismogenic coupling along the central San Andreas Fault. *Geophysical Research Letters*, *42*(2), 297–306. https://doi.org/10.1002/2014gl062222

Julve, J., Barbot, S., Moreno, M., Tassara, A., Araya, R., Catalán, N., et al. (2023). Recurrence time and size of Chilean earthquakes influenced by geological structure. *Nature Geoscience*, *17*, 1–9. https://doi.org/10.1038/s41561-023-01327-8

Kaneko, Y., Fialko, Y., Sandwell, D. T., Tong, X., & Furuya, M. (2013). Interseismic deformation and creep along the central section of the North Anatolian fault (Turkey): InSAR observations and implications for rate-and-state friction properties. *Journal of Geophysical Research*, *118*(1), 316–331. https://doi.org/10.1029/2012JB009661

Kaproth, B. M., & Marone, C. (2013). Slow earthquakes, preseismic velocity changes, and the origin of slow frictional stick-slip. *Science*, *341*(6151), 1229–1232. https://doi.org/10.1126/science.1239577

Khoshmanesh, M., & Shirzaei, M. (2018). Episodic creep events on the San Andreas Fault caused by pore pressure variations. *Nature Geoscience*, *11*(8), 610–614. https://doi.org/10.1038/s41561-018-0160-2

Khoshmanesh, M., Shirzaei, M., & Nadeau, R. (2015). Time-dependent model of aseismic slip on the central San Andreas Fault from InSAR time series and repeating earthquakes. *Journal of Geophysical Research*, *120*(9), 6658–6679. https://doi.org/10.1002/2015JB012039

Kronenberg, A. K., Kirby, S. H., & Pinkston, J. (1990). Basal slip and mechanical anisotropy of biotite. *Journal of Geophysical Research*, *95*(B12), 19257–19278. https://doi.org/10.1029/JB095iB12p19257

Lapusta, N., & Rice, J. R. (2003). Nucleation and early seismic propagation of small and large events in a crustal earthquake model. *Journal of Geophysical Research*, *108*(B4), 2205. https://doi.org/10.1029/2001jb000793

Latour, S., Schubnel, A., Nielsen, S., Madariaga, R., & Vinciguerra, S. (2013). Characterization of nucleation during laboratory earthquakes. *Geophysical Research Letters*, *40*(19), 5064–5069. https://doi.org/10.1002/grl.50974

Li, Y., Nocquet, J.-M., Shan, X., & Song, X. (2021). Geodetic observations of shallow creep on the Laohushan-Haiyuan fault, northeastern Tibet. *Journal of Geophysical Research*, *126*(6), e2020JB021576. https://doi.org/10.1029/2020JB021576

Linker, M. H., & Dieterich, J. H. (1992). Effects of variable normal stress on rock friction: Observations and constitutive relations. *Journal of Geophysical Research*, *97*(B4), 4923–4940. https://doi.org/10.1029/92JB00017

Liu, Y., & He, C. (2020). Friction properties of hornblende and implications for slow-slip events in subduction zones. *Tectonophysics*, *796*, 228644. https://doi.org/10.1016/j.tecto.2020.228644

Liu, Y., McGuire, J. J., & Behn, M. D. (2020). Aseismic transient slip on the Gofar transform fault, East Pacific Rise. *Proceedings of the National Academy of Sciences*, *117*(19), 10188–10194. https://doi.org/10.1073/pnas.1913625117

Lockner, D. A., Morrow, C., Moore, D., & Hickman, S. (2011). Low strength of deep San Andreas fault gouge from SAFOD core. *Nature*, *472*(7341), 82–86. https://doi.org/10.1038/nature09927

Mares, V. M., & Kronenberg, A. (1993). Experimental deformation of muscovite. *Journal of Structural Geology*, *15*(9–10), 1061–1075. https://doi.org/10.1016/0191-8141(93)90156-5

Mariani, E., Brodie, K. H., & Rutter, E. H. (2006). Experimental deformation of muscovite shear zones at high temperatures under hydrothermal conditions and the strength of phyllosilicate-bearing faults in nature. *Journal of Structural Geology*, *28*(9), 1569–1587. https://doi.org/10.1016/j.jsg.2006.06.009

Marone, C., Scholz, C. H., & Bilham, R. (1991). On the mechanics of earthquake afterslip. *Journal of Geophysical Research*, *96*(B5), 8441–8452. https://doi.org/10.1029/91JB00275

Marty, N. C., Claret, F., Lassin, A., Tremosa, J., Blanc, P., Madé, B., et al. (2015). A database of dissolution and precipitation rates for clay-rocks minerals. *Applied Geochemistry*, *55*, 108–118. https://doi.org/10.1016/j.apgeochem.2014.10.012

Matsuzawa, T., Hirose, H., Shibazaki, B., & Obara, K. (2010). Modeling short- and long-term slow slip events in the seismic cycles of large subduction earthquakes. *Journal of Geophysical Research*, *115*(B12), B12301. https://doi.org/10.1029/2010JB007566

McLaskey, G. C. (2019). Earthquake initiation from laboratory observations and implications for foreshocks. *Journal of Geophysical Research*, *124*(12), 12882–12904. https://doi.org/10.1029/2019JB018363

Moore, D. E., & Lockner, D. A. (2008). Talc friction in the temperature range 25°–400°C: Relevance for fault-zone weakening. *Tectonophysics*, *449*(1–4), 120–132. https://doi.org/10.1016/j.tecto.2007.11.039

Moore, D. E., Lockner, D. A., & Hickman, S. (2016). Hydrothermal frictional strengths of rock and mineral samples relevant to the creeping section of the San Andreas Fault. *Journal of Structural Geology*, *89*, 153–167. https://doi.org/10.1016/j.jsg.2016.06.005

Nakatani, M. (2001). Conceptual and physical clarification of rate and state friction: Frictional sliding as a thermally activated rheology. *Journal of Geophysical Research*, *106*(B7), 13347–13380. https://doi.org/10.1029/2000JB900453

Nie, S., & Barbot, S. (2021). Seismogenic and tremorgenic slow slip near the stability transition of frictional sliding. *Earth and Planetary Science Letters*, *569*, 117037. https://doi.org/10.1016/j.epsl.2021.117037

Nie, S., & Barbot, S. (2022). Rupture styles linked to recurrence patterns in seismic cycles with a compliant fault zone. *Earth and Planetary Science Letters*, *591*, 117593. https://doi.org/10.1016/j.epsl.2022.117593

Nie, S., & Barbot, S. (2024). Velocity and temperature dependence of steady-state friction of natural gouge controlled by competing healing mechanisms [Dataset]. *Zenodo*. https://doi.org/10.5281/zenodo.11004553

Niemeijer, A., Boulton, C., Toy, V., Townend, J., & Sutherland, R. (2016). Large-displacement, hydrothermal frictional properties of DFDP-1 fault rocks, Alpine Fault, New Zealand: Implications for deep rupture propagation. *Journal of Geophysical Research*, *121*(2), 624–647. https://doi.org/10.1002/2015JB012593

Niemeijer, A., Spiers, C., & Bos, B. (2002). Compaction creep of quartz sand at 400–600°C: Experimental evidence for dissolution-controlled pressure solution. *Earth and Planetary Science Letters*, *195*(3–4), 261–275. https://doi.org/10.1016/S0012-821X(01)00593-3

Ohnaka, M., & Shen, L.-F. (1999). Scaling of the shear rupture process from nucleation to dynamic propagation: Implications of geometric irregularity of the rupturing surfaces. *Journal of Geophysical Research*, *104*(B1), 817–844. https://doi.org/10.1029/1998jb900007

Okubo, P. G. (1989). Dynamic rupture modeling with laboratory-derived constitutive relations. *Journal of Geophysical Research*, *94*(B9), 12321–12335. https://doi.org/10.1029/JB094iB09p12321

Okuda, H., Niemeijer, A. R., Takahashi, M., Yamaguchi, A., & Spiers, C. J. (2023). Hydrothermal friction experiments on simulated basaltic fault gouge and implications for megathrust earthquakes. *Journal of Geophysical Research*, *128*(1), e2022JB025072. https://doi.org/10.1029/2022JB025072

Pozzi, G., Collettini, C., Scuderi, M., Tesei, T., Marone, C., Amodio, A., & Cocco, M. (2023). Fabric controls fault stability in serpentinite gouges. *Geophysical Journal International*, *235*(2), 1778–1797. https://doi.org/10.1093/gji/ggad322

Putnis, A., & Mauthe, G. (2001). The effect of pore size on cementation in porous rocks. *Geofluids*, *1*(1), 37–41. https://doi.org/10.1046/j.1468-8123.2001.11001.x

Qiu, Q., Barbot, S., Wang, T., & Wei, S. (2020). Slip complementarity and triggering between the foreshock, mainshock, and afterslip of the 2019 Ridgecrest rupture sequence. *Bulletin of the Seismological Society of America*, *110*(4), 1701–1715. https://doi.org/10.1785/0120200037

Qiu, Q., Hill, E. M., Barbot, S., Hubbard, J., Feng, W., Lindsey, E. O., et al. (2016). The mechanism of partial rupture of a locked megathrust: The role of fault morphology. *Geology*, *44*(10), 875–878. https://doi.org/10.1130/G38178.1

Ragon, T., Simons, M., Bletery, Q., Cavalié, O., & Fielding, E. (2021). A stochastic view of the 2020 Elazığ Mw 6.8 earthquake (Turkey). *Geophysical Research Letters*, *48*(3), e2020GL090704. https://doi.org/10.1029/2020GL090704

Rathbun, A. P., & Marone, C. (2013). Symmetry and the critical slip distance in rate and state friction laws. *Journal of Geophysical Research*, *118*(7), 3728–3741. https://doi.org/10.1002/jgrb.50224

Rice, J. R., & Ruina, A. L. (1983). Stability of steady frictional slipping. *Journal of Applied Mechanics*, *50*(2), 343–349. https://doi.org/10.1115/1.3167042

Rimstidt, J. D., & Barnes, H. (1980). The kinetics of silica-water reactions. *Geochimica et Cosmochimica Acta*, *44*(11), 1683–1699. https://doi.org/10.1016/0016-7037(80)90220-3

Ruina, A. (1983). Slip instability and state variable friction laws. *Journal of Geophysical Research*, *88*(B12), 10359–10370. https://doi.org/10.1029/JB088iB12p10359

Rutter, E., & Brodie, K. (2004a). Experimental grain size-sensitive flow of hot-pressed Brazilian quartz aggregates. *Journal of Structural Geology*, *26*(11), 2011–2023. https://doi.org/10.1016/j.jsg.2004.04.006

Rutter, E., & Brodie, K. (2004b). Experimental intracrystalline plastic flow in hot-pressed synthetic quartzite prepared from Brazilian quartz crystals. *Journal of Structural Geology*, *26*(2), 259–270. https://doi.org/10.1016/S0191-8141(03)00096-8

Rybacki, E., & Dresen, G. (2000). Dislocation and diffusion creep of synthetic anorthite aggregates. *Journal of Geophysical Research*, *105*(B11), 26017–26036. https://doi.org/10.1029/2000jb900223

Saffer, D. M., & Marone, C. (2003). Comparison of smectite-and illite-rich gouge frictional properties: Application to the updip limit of the seismogenic zone along subduction megathrusts. *Earth and Planetary Science Letters*, *215*(1–2), 219–235. https://doi.org/10.1016/S0012-821X(03)00424-2

Sathiakumar, S., & Barbot, S. (2021). The stop-start control of seismicity by fault bends along the Main Himalayan Thrust. *Communications Earth & Environment*, *2*(1), 1–11. https://doi.org/10.1038/s43247-021-00153-3

Scholz, C. H. (1998). Earthquakes and friction laws. *Nature*, *391*(6662), 37–42. https://doi.org/10.1038/34097

Scott, C., Bunds, M., Shirzaei, M., & Toke, N. (2020). Creep along the Central San Andreas Fault from surface fractures, topographic differencing, and InSAR. *Journal of Geophysical Research: Solid Earth*, *125*(10), e2020JB019762. https://doi.org/10.1029/2020jb019762

Shea, W. T., & Kronenberg, A. K. (1992). Rheology and deformation mechanisms of an isotropic mica schist. *Journal of Geophysical Research*, *97*(B11), 15201–15237. https://doi.org/10.1029/92JB00620

Shi, P., Wei, M., & Barbot, S. (2022). Contribution of viscoelastic stress to the synchronization of earthquake cycles on oceanic transform faults. *Journal of Geophysical Research*, *127*(8), e2022JB024069. https://doi.org/10.1029/2022JB024069

Shibazaki, B., Bu, S., Matsuzawa, T., & Hirose, H. (2010). Modeling the activity of short-term slow slip events along deep subduction interfaces beneath Shikoku, southwest Japan. *Journal of Geophysical Research*, *115*(B4), B00A19. https://doi.org/10.1029/2008JB006057

Skarbek, R. M., & Savage, H. M. (2019). RSFit3000: A MATLAB GUI-based program for determining rate and state frictional parameters from experimental data. *Geosphere*, *15*(5), 1665–1676. https://doi.org/10.1130/ges02122.1

Sleep, N. H. (1994). Grain size and chemical controls on the ductile properties of mostly frictional faults at low-temperature hydrothermal conditions. *Pure and Applied Geophysics*, *143*(1–3), 41–60. https://doi.org/10.1007/BF00874323

Sleep, N. H. (2006). Real contacts and evolution laws for rate and state friction. *Geochemistry, Geophysics, Geosystems*, *7*(8), Q08012. https://doi.org/10.1029/2005GC001187

Tesei, T., Collettini, C., Barchi, M. R., Carpenter, B. M., & Di Stefano, G. (2014). Heterogeneous strength and fault zone complexity of carbonate-bearing thrusts with possible implications for seismicity. *Earth and Planetary Science Letters*, *408*, 307–318. https://doi.org/10.1016/j.epsl.2014.10.021

Thurber, C., Roecker, S., Zhang, H., Baher, S., & Ellsworth, W. (2004). Fine-scale structure of the San Andreas fault zone and location of the SAFOD target earthquakes. *Journal of Geophysical Research*, *31*(12), L12S02. https://doi.org/10.1029/2003gl019398

Tian, P., & He, C. (2019). Velocity weakening of simulated augite gouge at hydrothermal conditions: Implications for frictional slip of pyroxene-bearing mafic lower crust. *Journal of Geophysical Research*, *124*(7), 6428–6451. https://doi.org/10.1029/2018JB016456

Titus, S. J., DeMets, C., & Tikoff, B. (2006). Thirty-five-year creep rates for the creeping segment of the San Andreas fault and the effects of the 2004 Parkfield earthquake: Constraints from alignment arrays, continuous global positioning system, and creepmeters. *Bulletin of the Seismological Society of America*, *96*(4B), S250–S268. https://doi.org/10.1785/0120050811

Tse, S. T., & Rice, J. R. (1986). Crustal earthquake instability in relation to the depth variation of frictional slip properties. *Journal of Geophysical Research*, *91*(B9), 9452–9472. https://doi.org/10.1029/JB091iB09p09452

Valdez, II, R., Kitajima, H., & Saffer, D. (2019). Effects of temperature on the frictional behavior of material from the Alpine Fault Zone, New Zealand. *Tectonophysics*, *762*, 17–27. https://doi.org/10.1016/j.tecto.2019.04.022

Veedu, D., & Barbot, S. (2016). The Parkfield tremors reveal slow and fast ruptures on the same asperity. *Nature*, *532*(7599), 361–365. https://doi.org/10.1038/nature17190

Wang, B., & Barbot, S. (2023). Pulse-like ruptures, seismic swarms, and tremorgenic slow-slip events with thermally activated friction. *Earth and Planetary Science Letters*, *603*, 117983. https://doi.org/10.1016/j.epsl.2022.117983

Wei, M., Kaneko, Y., Liu, Y., & McGuire, J. J. (2013). Episodic fault creep events in California controlled by shallow frictional heterogeneity. *Nature Geoscience*, *6*(7), 566–570. https://doi.org/10.1038/ngeo1835

Zhang, L., He, C., Liu, Y., & Lin, J. (2017). Frictional properties of the South China Sea oceanic basalt and implications for strength of the Manila subduction seismogenic zone. *Marine Geology*, *394*, 16–29. https://doi.org/10.1016/j.margeo.2017.05.006

Zoback, M., Hickman, S., & Ellsworth, W. (2010). Scientific drilling into the San Andreas fault zone. *Eos, Transactions American Geophysical Union*, *91*(22), 197–199. https://doi.org/10.1029/2010eo220001

Zoback, M., Hickman, S., Ellsworth, W., & the SAFOD Science Team. (2011). Scientific drilling into the San Andreas fault zone–an overview of SAFOD's first five years. *Scientific Drilling*, *11*, 14–28. https://doi.org/10.2204/iodp.sd.11.02.2011